ADVANCED MATERIALS
www.advmat.de

Dual Oxidation Suppression in Lead-Free Perovskites for Low-Threshold and Long-Lifespan Lasing

*Yahui Li, Zhenzhu Li, Yanxin Han, Runchen Lai, Jingjing Yao, Cunquan Li, Ming Xia, Hongzhi Zhou, Xin Sheng, Baini Li, Yiling Zhang, Tianyu Wang, Xiaohuo Shi, Jianwei Zhao, Yunfan Guo, Xiaoze Liu, Aron Walsh, and Enzheng Shi**

Low lasing threshold and long-term operational stability are essential in advancing cost-effective, efficient lead-free (tin) halide perovskite lasers. However, the rapid crystallization of tin perovskites and oxidation of Sn^{2+} lead to substantial amounts of lattice defects, detrimental to laser performance enhancement. Herein, a dual oxidation suppression strategy is developed to suppress the oxidation of Sn^{2+} 2D tin halide perovskites, i.e., adopting an oxygen-free two-step growth to enhance the crystal quality and incorporating electron-donating biuret molecules to coordinate with Sn^{2+} during the crystal growth, which led to the substantial reduction of lasing threshold to <1 μJ cm^{-2} in $(PEA)_2MASn_2I_7$. This represents the lowest value in lead-free perovskite nanolasers and approximately one order of magnitude lower than those previously reported for tin-based nanolasers. Investigations into the spontaneous photoluminescence (PL) and stimulated lasing emission revealed that 2D tin perovskites exhibited superior photostability and lasing stability compared to their lead counterparts. Specifically, the lasing intensity of $(PEA)_2MA_2Sn_3I_{10}$ constantly increased by >300% under optical pumping and the lasing threshold decreased by ≈17%, which is not observed in their lead counterparts. The findings highlight the prospect of 2D tin halide perovskites as lead-free gain materials and cavities for solution-processed nanolasers with low lasing thresholds and exceptional stability.

1. Introduction

Halide perovskites have emerged as promising candidates for future semiconductor lasers because of their excellent optoelectronic properties, direct-bandgap characteristics, high tunability in lattice constants and bandgaps, and low processing costs.[1–13] Compared to 3D perovskites, 2D halide perovskites exhibit superior stability, fewer surface defects, and intrinsic quantum-well structures.[14–18] Engineering the slab thickness (n) of 2D halide perovskites, typically in the Ruddlesden–Popper phase ($L_2A_{n-1}M_nX_{3n+1}$, where L, A, M, X, and n denote the spacer organic cation, small organic cation, metal cation, halide anion, and the number of metal halide octahedral layers in monolayer perovskite, respectively), provides a reliable and versatile strategy to achieve wide tunability in the lasing emission wavelength.[8,10] In addition, given their lower toxicity and smaller bandgap than lead perovskites, 2D tin halide perovskites

Y. Li
School of Materials Science & Engineering
Zhejiang University
Hangzhou 310027, China

Y. Li, Y. Han, C. Li, M. Xia, X. Sheng, B. Li, Y. Zhang, T. Wang, E. Shi
Research Center for Industries of the Future and School of Engineering
Westlake University
Hangzhou 310030, China
E-mail: shienzheng@westlake.edu.cn

Z. Li, A. Walsh
Department of Materials
Imperial College London
London SW7 2AZ, UK

R. Lai, X. Shi
Key Laboratory of Precise Synthesis of Functional Molecules of Zhejiang Province, Instrumentation and Service Center for Molecular Sciences
Westlake University
Hangzhou 310030, China

J. Yao, X. Liu
School of Physics and Technology, Center for Nanoscience and Nanotechnology, and Key Laboratory of Artificial Micro-and Nanostructures of Ministry of Education
Wuhan University
Wuhan 430072, China

H. Zhou, Y. Guo
Department of Chemistry
Zhejiang University
Hangzhou 310058, China

J. Zhao
Shenzhen HUASUAN Technology Co., Ltd.
Shenzhen 518107, China

E. Shi
Division of Solar Energy Conversion and Catalysis at Westlake University
Zhejiang Baima Lake Laboratory Co., Ltd.
Hangzhou 310051, China

The ORCID identification number(s) for the author(s) of this article can be found under https://doi.org/10.1002/adma.202418931

DOI: 10.1002/adma.202418931

are particularly advantageous for developing lead-free red and near-infrared lasers. Our previous study demonstrated that 2D tin halide perovskites could be more easily pumped to lase than their lead counterparts, highlighting their great potential for laser applications.[8] However, the ease of oxidation and rapid crystallization of 2D tin halide perovskites raise significant concerns and challenges, impacting both the fundamental understanding and the operational lifespan of laser devices.[19] Various strategies have been employed to reduce the number of lattice defects and manage the crystallization kinetics in 2D tin perovskite polycrystalline thin films.[20–22] However, for 2D tin halide perovskite single crystals which are essential for developing nanolasers without external gratings or distributed Bragg reflector mirrors,[8,23] effective strategies to inhibit Sn^{2+} oxidation remain insufficient. Moreover, there is a lack of understanding regarding the emission stability of tin halide perovskite lasers. Compared to the environmental instability of 2D tin halide perovskites, which can be routinely resolved through mature encapsulation techniques, the assessment and improvement of light emission stability, including spontaneous PL and stimulated lasing emission, are more critical for developing long-lifespan lasers.

In this study, we mitigated the Sn^{2+} oxidation and increased the size of 2D tin halide perovskite single crystals by incorporating electron-donating biuret molecules and adopting a two-step growth strategy in an oxygen-free atmosphere. The optically pumped nanolasers based on these 2D perovskites possessed excellent lasing performance. Notably, $(PEA)_2MASn_2I_7$ exhibited the lowest lasing threshold of 0.88 μJ cm^{-2}, approximately one order of magnitude lower than those of previously reported tin-based nanolasers. In addition, a comprehensive investigation into both the spontaneous PL and stimulated lasing emission revealed that 2D tin-based perovskites possessed superior photostability and lasing stability compared to their lead-based counterparts. For instance, the lasing emission of $(PEA)_2MA_2Sn_3I_{10}$ increased by >300% under a constant pumping fluence of 1.1 P_{th}, whereas that of $(PEA)_2MA_2Pb_3I_{10}$ decreased to 80%. Meanwhile, the lasing threshold of $(PEA)_2MA_2Sn_3I_{10}$ nanolasers was lowered after the optical pumping.

1.1. Lead-Free Perovskite Lasing Performance and Cavity Tuning

To grow 2D tin halide perovskite bulk single crystals with minimal oxidation defects, we introduced biuret molecules with strong electron-donating ability and synthesized single crystals in an oxygen-free atmosphere to inhibit the oxidation of Sn^{2+}. Additionally, instead of the commonly employed supersaturated solution precipitation method for 2D halide perovskite crystal growth,[24,25] we adopted a modified two-step growth strategy to reduce the nucleation density of 2D tin halide perovskites (Figure S1, Supporting Information, details discussed later). Reference crystals were synthesized without the addition of biuret, either in an N_2 -filled glovebox or in air, and were denoted as N_2 and air samples, respectively. Considering the fluctuation in lasing performance due to variations in the geometry and thickness of exfoliated flakes, statistical analyses of lasing tests were conducted on various exfoliated perovskite flakes (Figures S2–S19, Supporting Information). Optically pumped $(PEA)_2MA_{n-1}Sn_nI_{3n+1}$ perovskite flakes possessed tunable and sharp lasing emission ranging from ≈660 to ≈800 nm. For example, $(PEA)_2MA_2Sn_3I_{10}$ flakes displayed a minimum full width at half maximum (FWHM) of ≈0.35 nm, corresponding to a high Q factor of ≈2000 (Figure S19, Supporting Information). The pump fluence-dependent PL spectra of $(PEA)_2MA_2Sn_3I_{10}$ revealed an initial broad spontaneous PL emission with an FWHM of ≈27 nm centered at ≈790 nm. As the pump fluence increased to 1.27 μJ cm^{-2}, multiple lasing peaks emerged at ≈800 nm, and the FWHM of the PL spectra sharply decreased to <1 nm (**Figures 1b,c** and S19, Supporting Information). This correlation between the pump fluence and FWHM remained consistent from $(PEA)_2SnI_4$ to $(PEA)_2MA_2Sn_3I_{10}$ (Figures S2–S19, Supporting Information). The lasing thresholds for $(PEA)_2MASn_2I_7$ and $(PEA)_2MA_2Sn_3I_{10}$ were lower compared to $(PEA)_2SnI_4$, due to the weaker exciton-phonon coupling strength in 2D perovskites with higher n values.[8,10,26] In addition, we compared the polarization of the lasing emission and spontaneous PL emission to further validate the lasing emission (Figure 1d). Notably, while the spontaneous PL emission is random, the lasing emission exhibits strong polarization, with a degree of polarization (DOP) of 95% ($DOP = (I_{max}–I_{min})/(I_{max}+I_{min})$, I_{max} is the maximum intensity at ≈0° and I_{min} is the minimum intensity at ≈90°).

Moreover, the lasing threshold (P_{th}) serves as a crucial metric for laser performance assessment. As revealed from the comparison between the samples with biuret and reference samples (Figure 1e), $(PEA)_2MA_{n-1}Sn_nI_{3n+1}$ (n = 1-3) with biuret presented the smallest fluctuation in threshold values. The order of lasing threshold is $P_{th}(Sample_{Air}) > P_{th}(Sample_{N2}) > P_{th}(Sample_{biuret})$. Among all the measured samples, the lowest lasing threshold was as low as 0.88 μJ cm^{-2} (n = 2, Figure S13, Supporting Information), one order of magnitude lower than that of our previous report,[8] due to our optimized growth processes and more stringent preparation control. For $(PEA)_2SnI_4$ nanolasers, the lasing threshold was also much smaller than our previous report and the layered nanowire lasers reported recently.[2,8] In addition, the lasing thresholds of the nanolasers based on 2D tin halide perovskite obtained from two-step growth were lower than those of single crystals prepared using the one-step method (Figures S20–S22, Supporting Information), and those of their lead counterparts (Figures S23 and S24, Supporting Information), implying the two-step crystal nucleation and growth reduce the trap states and improve the crystal quality. Simultaneously, we achieved single-mode lasing on a $(PEA)_2MASn_2I_7$ synthesized with a biuret single crystal nanosheet with an edge length of 3.4 μm × 1.9 μm. As the edge length increases, the number of lasing modes progressively increases[27,28] (Figure S25, Supporting Information).

For the optically pumped nanolasers herein, the exfoliated 2D halide perovskite flakes simultaneously served as gain materials and resonance cavities. The resonance mode of these nanolasers, either Fabry–Perot (FP) mode or Whispering Gallery (WGM) mode, is primarily determined by the external geometry of the 2D halide perovskite flakes.[29] Specifically, $(PEA)_2SnI_4$ flakes were chosen for demonstration due to their visible lasing emission and ease of imaging by the CCD camera. Figure 1f and Figure S26 (Supporting Information) show lasing images of exfoliated flakes obtained in either FP or WGM mode. However, these exfoliated flakes generally possess random geometries, complicating

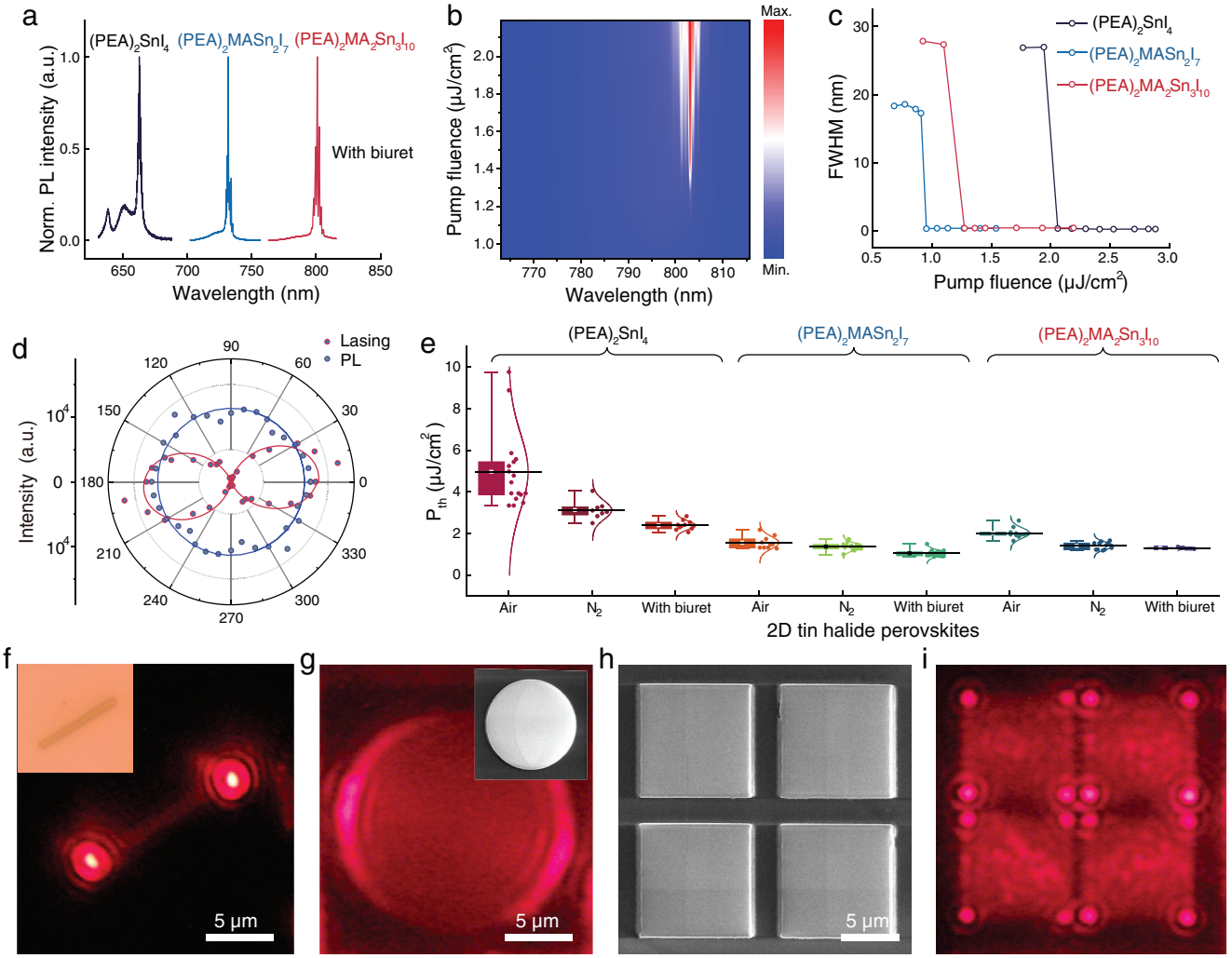

Figure 1. Lasing performance of $(PEA)_2MA_{n-1}Sn_nI_{3n+1}$ (n = 1–3) flakes and the control of cavities via nanofabrication. a) Lasing spectra of $(PEA)_2SnI_4$ at 2.88 μJ cm^{-2}, $(PEA)_2MASn_2I_7$ at 1.54 μJ cm^{-2} and $(PEA)_2MA_2Sn_3I_{10}$ at 2.19 μJ cm^{-2}. b) 2D mapping of $(PEA)_2MA_2Sn_3I_{10}$ PL spectra associated with the excitation pump fluence. c) The FWHM as a function of the pump fluence of $(PEA)_2MA_{n-1}Sn_nI_{3n+1}$ (n = 1–3) nanolasers. d) Polarization-resolved spectra of both the lasing (red) and PL (blue) of $(PEA)_2MA_2Sn_3I_{10}$ nanolasers. e) Lasing thresholds of nanolasers based on 2D tin halide perovskite synthesized in air, N_2, and with biuret. f) The lasing image of an exfoliated $(PEA)_2SnI_4$ flake with a well-defined nanowire morphology. The inset is the corresponding optical image. g) The lasing image of a circular $(PEA)_2SnI_4$ nanosheet fabricated via FIB etching. The inset is the corresponding SEM image. The SEM (h) and lasing (i) images of a highly periodic $(PEA)_2SnI_4$ array fabricated by FIB etching.

the control of the resonance modes. To address this challenge, we employed focused ion beam (FIB) lithography with a finely controllable ion exposure dosage to fabricate patterned cavities with well-defined geometries on exfoliated 2D tin perovskite flakes. As shown in Figure 1g, a circular $(PEA)_2SnI_4$ nanosheet was successfully fabricated, exhibiting typical WGM resonance mode. Furthermore, a highly periodic $(PEA)_2SnI_4$ array with square geometry (≈10 μm in length) was successfully prepared (Figure 1h,i and Figures S27 and S28, Supporting Information). By exciting these fabricated squares, we observed strong lasing emission from the four corners of these squares, a typical characteristic of optically pumped lasers in WGM mode, consistent with the simulated electric field distributions (Figure 4h; Figure S28, Supporting Information). The successful demonstration of cavity design via nanofabrication techniques highlights the controllable modulation of the lasing emission of 2D tin halide perovskite nanolasers.

1.2. Growth of Large-Size Single Crystal Following Dual Oxidation Suppression Strategy

The modified two-step synthetic strategy produced 2D tin halide perovskite bulk single crystals with a larger size (≈4 mm), whereas the conventional one-step method yielded numerous small crystals (**Figure 2a**). This is because the crystal growth at the 2nd step was initiated from an undissolved seed crystal in a low concentration rather than high-density homogeneous nucleation in the conventional crystal growth. The larger crystal size facilitated the exfoliation of bulk crystals into thin flakes,

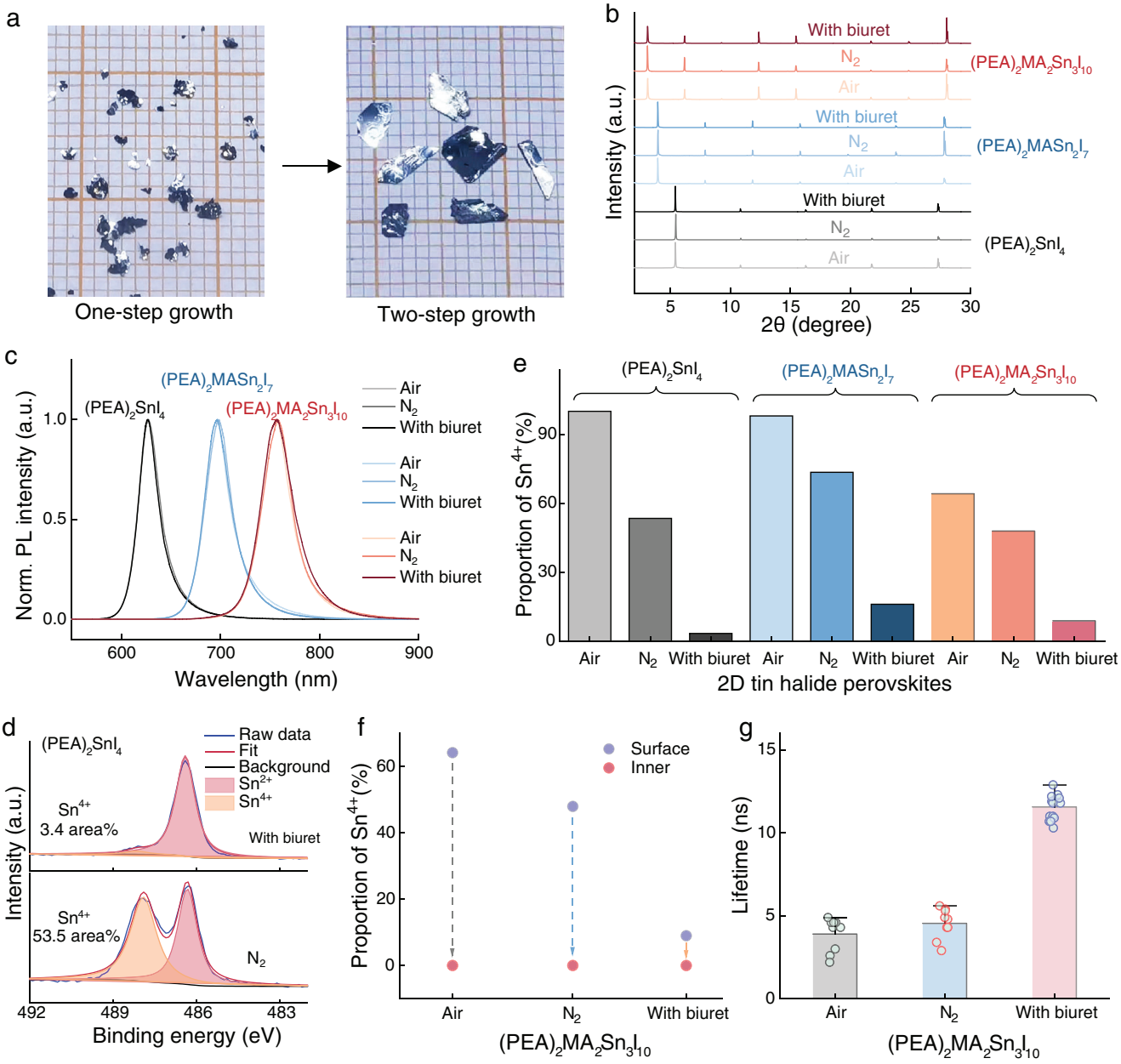

Figure 2. Optimized single crystal quality and dual oxidation suppression of Sn^{2+} via the biuret-assisted two-step growth strategy in an oxygen-free atmosphere. a) Photographs of $(PEA)_2MA_2Sn_3I_{10}$ single crystals obtained via one-step and modified two-step synthesis methods. The length of the red square is 1 mm. PXRD profiles (b) and PL spectra (c) of $(PEA)_2MA_{n-1}Sn_nI_{3n+1}$ (n = 1–3) synthesized in air, N_2, and with biuret. d) XPS core level spectra of Sn 3*d* for $(PEA)_2SnI_4$ in N_2 and with biuret. e) Proportion of Sn^{4+} measured from the surface of $(PEA)_2MA_{n-1}Sn_nI_{3n+1}$ (n = 1-3) crystals synthesized in air, N_2 and with biuret. f) Proportion of Sn^{4+} on the surface and the inner area of $(PEA)_2MA_2Sn_3I_{10}$ synthesized in air, N_2, and with biuret. g) Lifetime ($\tau 2$) of $(PEA)_2MA_2Sn_3I_{10}$ synthesized in air, N_2 and with biuret.

and the dissolution and recrystallization during the two-step growth extended the crystal growth time and reduced defects within the crystal lattice. Powder X-ray diffraction (XRD) profiles of $(PEA)_2MA_{n-1}Sn_nI_{3n+1}$ under three different growth conditions revealed that changes in the growth environment and the introduction of biuret did not alter the interlayer spacing of single crystals (Figure 2b). In addition, no detectable oxygen signal was found from the energy-dispersive spectroscopy (EDS) mapping of exfoliated $(PEA)_2MA_{n-1}Sn_nI_{3n+1}$ single crystal nanosheets synthesized with biuret, suggesting that the biuret did not incorporate into the perovskite lattice (Figures S29–S31, Supporting Information). Furthermore, steady-state PL and UV–vis spectroscopy characterizations confirmed that the optical gap of single crystals remained consistent across different preparation environments for the same n value (Figure S32, Supporting Information). From $(PEA)_2SnI_4$ to $(PEA)_2MA_2Sn_3I_{10}$, the PL peak consistently shifts from ≈627 to ≈758 nm (Figure 2c).

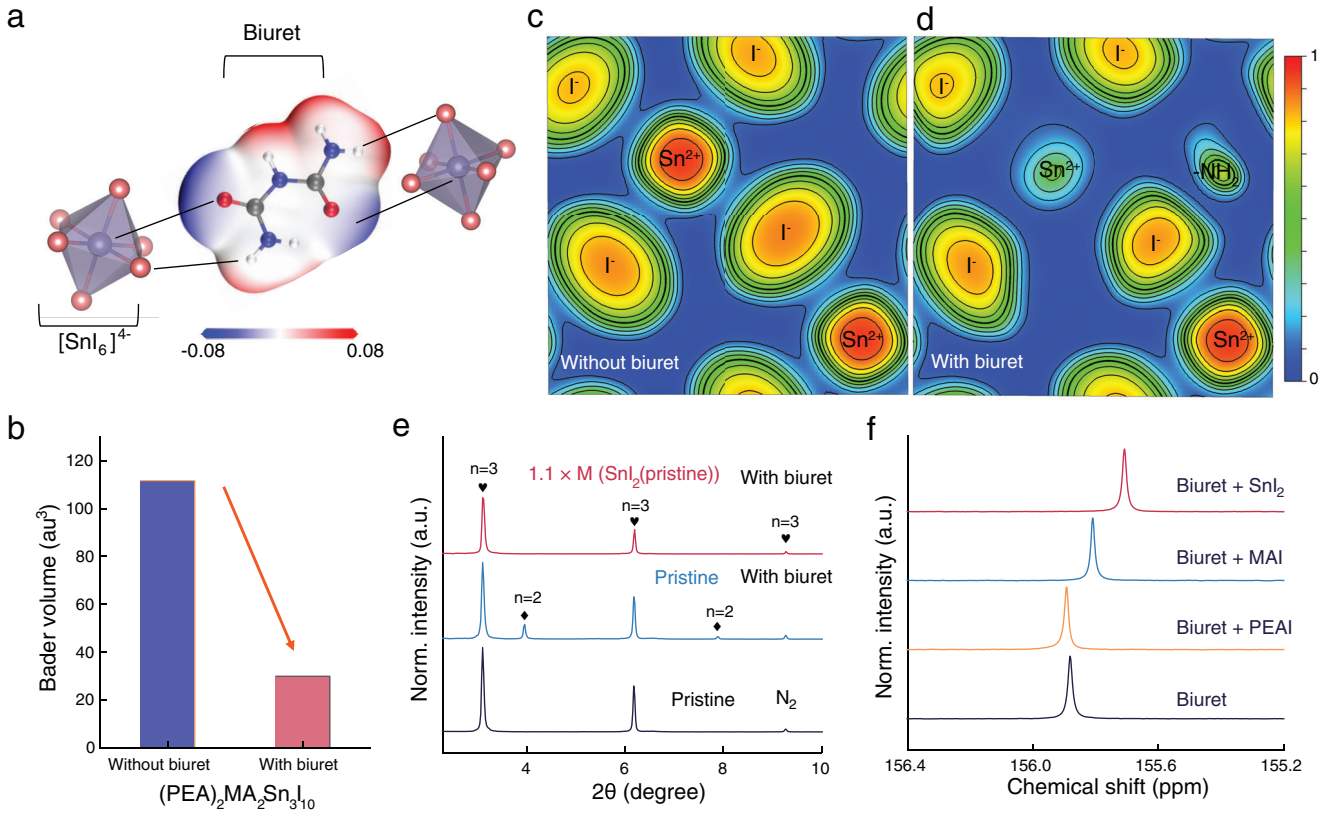

Figure 3. Stabilization mechanism of biuret molecules. a) ESP map of biuret molecule and its potential interaction with $[SnI_6]^{4-}$ octahedra. b) Bader volume of $(PEA)_2MA_2Sn_3I_{10}$ with and without the biuret. Electron localization function images of $(PEA)_2MA_2Sn_3I_{10}$ (c) without biuret and (d) with the biuret. e) XRD profiles of the $(PEA)_2MA_2Sn_3I_{10}$ products under N_2 without biuret (black), with biuret (blue), and with biuret & an additional 10% SnI_2 (red). f) ^{13}C NMR spectra of biuret, biuret + PEAI, biuret + MAI and biuret + SnI_2 in DMSO-d_6 solution.

For 2D tin halide perovskite single crystals grown in aqueous solutions, the crystal collection atmosphere impacts the surface state as the Sn^{2+} at the crystal surface is prone to oxidation ("surface" refers to the outermost region of the as-synthesized 2D tin perovskite single crystals collected directly from the growth solution without any treatment). XPS results revealed that the molar ratio of Sn^{4+} reached as high as ≈100% on the $(PEA)_2SnI_4$ single crystal surface when collected in air, but was suppressed to 53.5% when collected in N_2 (Figure 2d and Figure S33, Supporting Information). The remaining oxidation of Sn^{2+} could be attributed to the I_2 absorbed on the crystal surface or trace amounts of O_2 in the glovebox.[30] In comparison, biuret coordination during crystal growth reduced the Sn^{4+} content to 3.4% on the $(PEA)_2SnI_4$ surface (Figure 2d), demonstrating that biuret molecules with strong electron-donating ability effectively protected the surface of tin perovskites from oxidation during the crystal growth and collection processes, thereby inhibiting Sn^{4+} formation. XPS depth profile confirms that oxidation progresses from the surface inward (Figure S34, Supporting Information).

Comparisons of the Sn^{4+} content on 2D tin halide perovskite (n = 1–3) surfaces under different growth conditions indicated that the Sn^{4+} content on the biuret-assisted crystal surface was significantly lower than that on the other samples (Figure 2e and Figure S33, Supporting Information). However, the Sn^{4+} content inside all the single crystals under different growth conditions was extremely low. For example, in $(PEA)_2MA_2Sn_3I_{10}$, the inner crystal (>100 μm below the pristine surface) was exposed by removing the single crystal surface (Figure S35, Supporting Information), and the Sn^{4+} content of all crystals prepared under different growth conditions was almost undetectable. These results indicated that the oxidation of Sn^{2+} propagated from the surface to the interior regions (Figure 2f and Figure S36, Supporting Information). Therefore, by inhibiting the surface oxidation using a dual oxidation suppression strategy, we improved the spatial uniformity of the single crystals, justifying the lower lasing threshold and smaller fluctuations observed in the nanolasers based on biuret-protected crystals. Additionally, time-resolved PL measurements were conducted to determine the carrier lifetime of $(PEA)_2MA_2Sn_3I_{10}$ crystals synthesized under different growth conditions (Figures S37–S39, Supporting Information). By fitting the PL decay plots with a double-exponential curve, we found the extracted lifetime (τ_2) of the crystal with biuret (11.6 ns) was significantly longer than that of crystals grown in N_2 (4.6 ns) and air (3.9 ns) (Figure 2g). This finding indicates that biuret molecules significantly reduced the trap states within the tin perovskites, thereby rationalizing the lower lasing threshold in the nanolasers based on biuret-protected crystals.

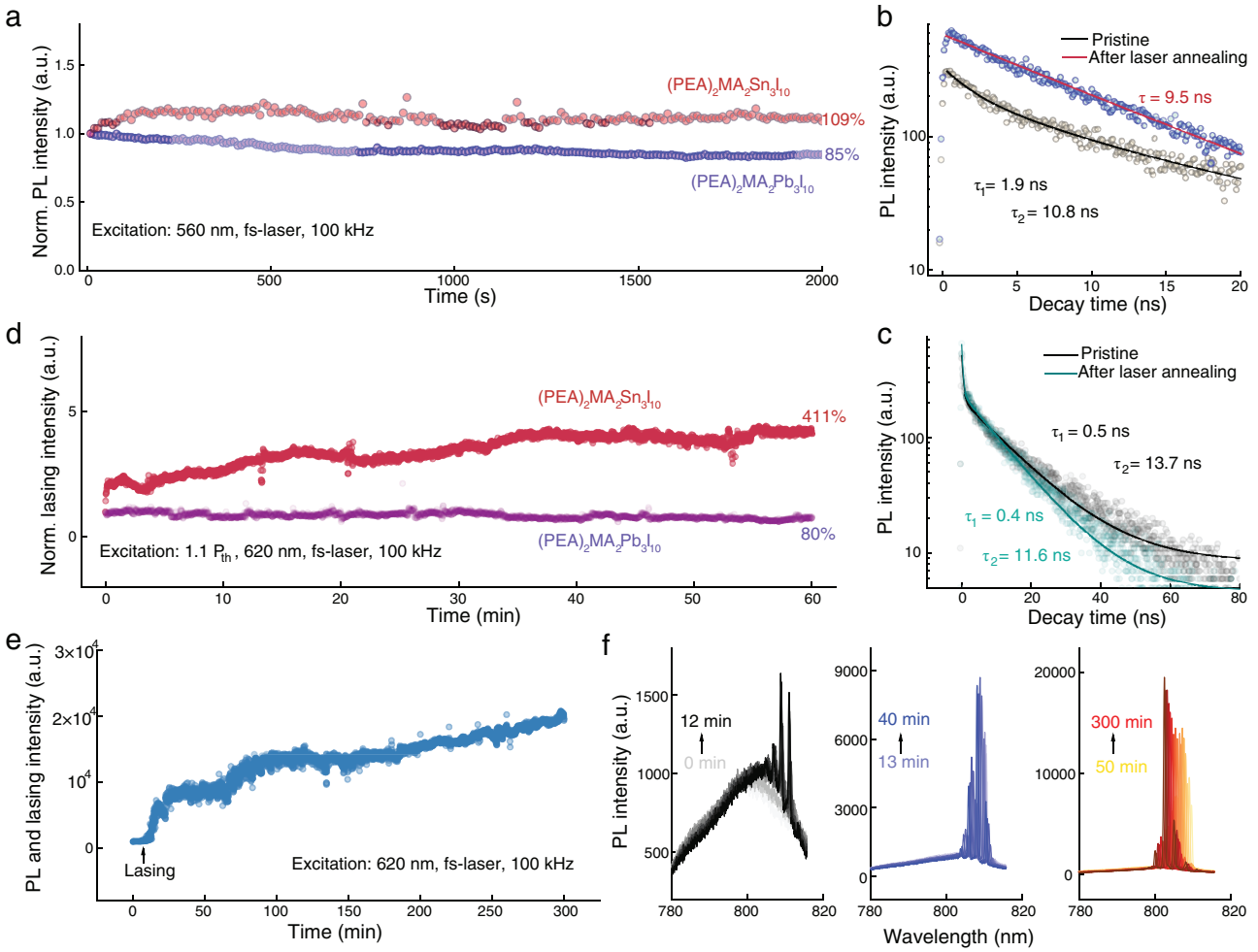

Figure 4. Photostability and lasing stability of 2D tin halide perovskites. a) PL retention of $(PEA)_2MA_2Pb_3I_{10}$, and $(PEA)_2MA_2Sn_3I_{10}$ at a pump fluence of 0.17 μJ cm^{-2}, both of which used 560 nm fs laser as the excitation light. b) Time-resolved PL spectra of $(PEA)_2MA_2Sn_3I_{10}$ at the pristine state and after laser illumination. c) Time-resolved PL spectra of $(PEA)_2MA_2Pb_3I_{10}$ in the pristine state and after laser illumination. d) Lasing stability of $(PEA)_2MA_2Pb_3I_{10}$ and $(PEA)_2MA_2Sn_3I_{10}$ at a pump fluence of 1.1 P_{th}, both of which use a 620 nm fs-laser as excitation light. e) Evolution of the light emission of a $(PEA)_2MA_2Sn_3I_{10}$ flake from spontaneous PL to lasing under constant optical pumping. f) Extracted PL and lasing spectra from (e) at different periods.

1.3. Stabilization Mechanism from Biuret Molecule Coordination

To better understand how the incorporation of biuret reduces the lasing threshold and minimizes Sn^{2+} oxidation, we conducted a series of simulations and spectroscopy characterizations. The simulated electrostatic potential (ESP) map of the biuret molecule reveals high electron density at the terminal oxygen, indicating its strong affinity for donating lone-pair electrons to coordinate with Sn^{2+}. Additionally, the terminal $-NH_2$ group with a positive static potentially interacts with I^- (**Figure 3a**). To further clarify the anti-oxidation mechanism of biuret molecules, Bader analysis of $(PEA)_2MA_2Sn_3I_{10}$ was performed. The optimized crystal structure, as illustrated in Figure S40 (Supporting Information), revealed a Sn—O bonding distance of 2.31 Å and H—I bonding distances of 2.81 and 2.84 Å, respectively. These values indicate the robust interaction between the biuret and tin perovskite single crystals. For $(PEA)_2MA_2Sn_3I_{10}$, the Bader volume of the outermost Sn atom is 112 au^3 in the single crystal without biuret, which decreases to 28 au^3 in the single crystal with biuret, indicating the significant stabilization of Sn^{2+} by biuret (Figure 3b). Furthermore, the electron localization function mapped the electron cloud in both pristine (without biuret) and biuret-protected 2D tin perovskite single crystals, revealing the strong electron localization of Sn^{2+} in the biuret-protected single crystal (Figure 3c,d).[22] In addition, by adding 0.2 mmol of biuret molecules into the growth solution for phase-pure $(PEA)_2MA_2Sn_3I_{10}$ crystals (N_2 atmosphere, see Methods), a considerable occurrence of the $(PEA)_2MASn_2I_7$ phase was observed in the nucleated products. However, the subsequent addition of 0.04 mmol of SnI_2 eliminated the n = 2 phase. This suggests a robust interaction between the biuret and SnI_2 (Figure 3e) during crystal growth. Moreover, from the ^{13}C nuclear magnetic resonance (NMR) spectroscopy (Figure 3f), the resonance signal at δ = 155.88 ppm originating from the C=O group in biuret underwent chemical shifts of $\Delta\delta \approx 0.07$ ppm and $\Delta\delta \approx 0.17$ ppm after interacting with MAI and SnI_2, respectively

(Figure 3f). This finding directly reveals that the interaction between the biuret and SnI_2 is stronger than that between the biuret and MAI, which could be attributed to the stronger Lewis acid-base interaction between Sn^{2+} and C═O,[20] thus beneficial to suppress the oxidation of Sn^{2+} in 2D tin halide perovskite crystals.[31]

1.4. Spontaneous PL Emission and Lasing Stability

By implementing the modified two-step growth strategy in an oxygen-free atmosphere and biuret coordination, we have obtained 2D tin halide perovskite single crystals with low oxidation levels and high spatial uniformity, laying the foundation to further investigate the stability of tin halide perovskites. To date, the existing understanding and studies of tin perovskite stability have primarily focused on their poor environmental stability, which is attributed to the ease of oxidation of Sn^{2+} into Sn^{4+}. However, comprehensive studies of their stability, including thermal, photo, spontaneous PL emission, and lasing stability, are still insufficient. In this study, we probed the light emission stability of 2D tin halide perovskites grown with biuret as well as their lead counterparts. As shown in **Figure 4a**, the PL intensity of $(PEA)_2MA_2Sn_3I_{10}$ after 2000 s excitation increased to 109% of the initial value (Figure 4a), and another two distinct $(PEA)_2MA_2Sn_3I_{10}$ samples exhibited similar excellent photostability (Figure S41, Supporting Information). In contrast, the PL retention rate of $(PEA)_2MA_2Pb_3I_{10}$ after equivalent illumination duration was reduced to 85% (Figure 4a and Figure S42, Supporting Information). As the optical gaps of tin perovskites are smaller than those of the corresponding lead perovskites, the energy difference ($\Delta E = h\nu - E_g$, $h\nu$: photon energy. E_g: optical gap) in tin perovskites under the same excitation light because the relaxation of hot carriers was larger than that of lead perovskite (Figure S43, Supporting Information), resulting in greater heat generation in tin halide perovskite. Too much-generated heat is usually detrimental to halide perovskites and accelerates their degradation.[32] Consequently, we can conclude that 2D tin halide perovskites exhibit superior photostability compared to their lead counterparts. This counterintuitive increase of the PL emission intensity in 2D tin perovskites was attributed to the laser illumination annealing effect,[9] as validated by the optimized carrier dynamics. As shown in Figure 4b, the photoexcited carriers in pristine $(PEA)_2MA_2Sn_3I_{10}$ before the test exhibited a biexponential decay process, comprising a fast decay process of 1.9 ns (τ_1) and a slow process of 10.8 ns (τ_2), and the fast process was usually induced by trap states.[33,34] After annealing by the femtosecond (fs) laser illumination, the intensity of PL_0 (t = 0) increased significantly (Figure 4b), consistent with the PL enhancement shown in Figure 4a. Meanwhile, the laser illumination annealing eliminated the fast decay process in the carrier dynamics of $(PEA)_2MA_2Sn_3I_{10}$, leaving a single-exponential decay (lifetime≈9.5 ns), indicating the annealing of trap defects. In contrast, both the PL decay curves in the pristine $(PEA)_2MA_2Pb_3I_{10}$ and after laser illumination exhibited a biexponential decay process, with a fast decay process of 0.5 ns and a slow decay process of 13.7 ns for the pristine state and a fast decay process of 0.4 ns and a slow decay process of 11.6 ns after laser illumination (Figure 4c).

In addition, we monitored the lasing stability of 2D lead and tin halide perovskites. The lasing emission intensity of the $(PEA)_2MA_2Pb_3I_{10}$ flake decayed to 80% in ≈60 min under a pumping fluence of 1.1 P_{th}, and decayed to 50% in ≈50 min under 1.3 P_{th} (Figure 4b and Figure S44, Supporting Information). In comparison, $(PEA)_2MA_2Sn_3I_{10}$ exhibited evolutionary and gradually improved lasing performance. As shown in Figure 4d, the lasing emission intensity of $(PEA)_2MA_2Sn_3I_{10}$ showed no decay over time under 1.1 P_{th}, and even increased by >300% during the pumping period (411% after 60 min, Figure 4d). To further demonstrate the laser illumination annealing effect on the light emission properties of $(PEA)_2MA_2Sn_3I_{10}$, we excited one exfoliated flake under a fluence below P_{th} and monitored the evolution of the PL emission. Initially, only spontaneous PL was observed (Figure 4e,f). After continuously exciting the flake for ≈7 min, we observed the emergence of a clear lasing signal. Within the following ≈20 min, the lasing emission intensity increased dramatically to ≈5 times the initial PL intensity. The lasing emission continued to increase steadily for the following ≈270 min (≈6.75×10^8 pulses), with the lasing intensity reaching 20 000 counts, ≈20 times the initial PL intensity. As a result, the laser illumination annealing effect led to a reduction in the lasing threshold (by ≈17%, Figures S45 and S46, Supporting Information). Under laser illumination annealing, the reduction of defects decreases the number of carriers trapped by defects and suppresses non-radiative recombination.[9,35] This leads to an increase in carrier density, thereby enhancing the lasing intensity. The observed blue shift in the lasing wavelength during laser illumination may arise from the Burstein-Moss effect (increased carrier density broadens the effective bandgap, resulting in a blue shift of the lasing peak)[36] or Drude model (higher carrier density reduces the refractive index below the bandgap and the decrease in refractive index induces a blue shift in the lasing wavelength, based on the fact that the resonant wavelength is proportional to the refractive index in the WGM cavity).[37–39] Similar to the above photostability measurements, the heat generation due to the relaxation of hot carriers in tin halide perovskites was greater than that in lead perovskites during the lasing stability testing (Figure S47, Supporting Information), which validates the better lasing stability of 2D tin halide perovskites over their lead counterparts. Moreover, the laser illumination annealing phenomenon was observed not only in $(PEA)_2MA_2Sn_3I_{10}$ but also in $(PEA)_2MASn_2I_7$. The increased lasing emission could be maintained even after the 2D tin perovskite flakes underwent heating (80 K to 300 K) →re-cooling (300 K to 80 K) cycles (Figure S48, Supporting Information). Then we systematically investigated the temperature-dependent lasing behavior of $(PEA)_2MASn_2I_7$ (Figure S49, Supporting Information). As the temperature increases gradually, the lasing threshold increases accordingly. By fitting the lasing threshold-temperature relationship following the formula $P_{th}(T) = P_0 \times \exp(\frac{T}{T_c})$, where P_0 is the lasing threshold at 0 K and T_c is the characteristic temperature, the T_c was determined to be 65 K, which is higher than the reported T_c for 2D n = 1 tin perovskite,[11] and lower than that of $CsPbBr_3$.[27] The flakes could still preserve a strong lasing emission after being placed in an N_2 glovebox for 4 months, indicating the robustness of 2D tin halide perovskite nanolasers under stringent encapsulation (Figures S50–S52, Supporting Information).

2. Conclusion

In conclusion, by incorporating electron-donating biuret molecules and employing an in situ two-step growth strategy in an oxygen-free atmosphere, we effectively improved the crystal quality, and size and suppressed the oxidation of Sn^{2+} in 2D tin halide perovskite single crystals. These advancements enabled the creation of 2D lead-free halide perovskite nanolasers with remarkably low lasing thresholds and excellent light emission stability. Future efforts should focus on further enhancing material stability and implementing better thermal management to achieve continuous wave lasing. In addition, the photophysics revealing the high photo and lasing stability of nanolasers based on 2D tin halide perovskites also need to be elaborated more systematically.

3. Experimental Section

Materials: Phenethylammonium iodide (PEAI), and methylammonium iodide (MAI) were purchased from Greatcell Solar Materials. Tin (II) iodide (SnI_2) and biuret were purchased from Shanghai Macklin Biochemical Technology Co., Ltd. Hydriodic acid (HI, 57 wt.%) was purchased from Tokyo Chemical Industry. Hypophosphorous acid (H_3PO_2, 50 wt.%) was purchased from J&K Scientific Ltd. All the materials were used without further purification.

Synthesis of Single Crystals Under Different Conditions—$(PEA)_2MA_{n-1}Sn_nI_{3n+1}$ ($n = 1–3$) single crystals with biuret: For the $(PEA)_2SnI_4$ single crystal, 0.2 mmol of PEAI, 0.4 mmol of SnI_2, and 0.2 mmol of biuret were added to a glass vial containing 2 mL of HI and 0.2 mL of H_3PO_2. For $(PEA)_2MASn_2I_7$ ($(PEA)_2MA_2Sn_3I_{10}$), 0.17 mmol of PEAI, 0.40 mmol of MAI (0.67 mmol), 0.40 mmol of SnI_2 (0.44 mmol), and 0.2 mmol of biuret were added to a glass vial containing 2 mL of HI and 0.2 mL of H_3PO_2. After thorough dissolution in an N_2-filled glovebox, the cooling process was performed in the glovebox following the modified two-step method procedure shown in Figure S1 (Supporting Information). The weighing of raw materials, the addition of solvents, and the collection of single crystals were carried out in the N_2 glove box. During the collection of single crystals, it was necessary to ensure that the oxygen and water contents in the N_2 glove box were <5 ppm. The addition of H_3PO_2 ensures that the Sn^{4+} was fully reduced to Sn^{2+} during the synthesis.[40] After the acids were added, the glovebox was purged with high-purity N_2 for over 30 min immediately to minimize potential residual vapors from HI and H_3PO_2.

$(PEA)_2MA_{n-1}Sn_nI_{3n+1}$ ($n = 1–3$) single crystals in N_2: For $(PEA)_2SnI_4$ single crystals, 0.2 mmol of PEAI and 0.4 mmol of SnI_2 were added to a glass vial containing 2 mL of HI and 0.2 mL of H_3PO_2. For $(PEA)_2MASn_2I_7$ ($(PEA)_2MA_2Sn_3I_{10}$), 0.17 mmol of PEAI, 0.40 mmol of MAI (0.67 mmol) and 0.4 mmol of SnI_2 were added to a glass vial containing 2 mL of HI and 0.2 mL of H_3PO_2. The processes of single crystal growth and collection were the same as those of single crystals with biuret.

$(PEA)_2MA_{n-1}Sn_nI_{3n+1}$ ($n = 1–3$) single crystals in air: For $(PEA)_2SnI_4$ single crystals, 0.2 mmol of PEAI and 0.4 mmol of SnI_2 were added to a glass vial containing 2 mL of HI and 0.2 mL of H_3PO_2. For $(PEA)_2MASn_2I_7$ ($(PEA)_2MA_2Sn_3I_{10}$), 0.17 mmol of PEAI, 0.40 mmol of MAI (0.67 mmol), and 0.4 mmol of SnI_2 were added to a glass vial containing 2 mL of HI, and 0.2 mL of H_3PO_2. The weighing of raw materials, the addition of solvents, and the collection of single crystals were carried out in the air. The cooling process was the same as that of single crystals with biuret. Compared to the previous report,[8] the growth time at the first cooling was not only increased but also added an additional heating→re-cooling procedure (for details, see Figure S1, Supporting Information).

Lasing Test: A home-built microscope setup was used for laser spectroscopy measurements. The fundamental 1030 nm beam from Yb: KGW laser (Pharos, Light Conversion Ltd., 100 kHz) with a temporal resolution of 170 fs was imported into an optical parametric amplifier (Orpheus-HP, Light Conversion Ltd.) to generate excitation light with various wavelengths. The pump beam was focused onto mechanically exfoliated samples by a microscope with a 50× NIR objective (NA 0,20). A plano-convex lens with a focal length of 500 mm was placed in the light path to increase the light spot size to fully cover the sample to ensure the most effective excitation. The principle for sample selection was to avoid or minimize sharp angles while the samples were of similar thickness. The PL was filtered by a longpass filter and collected by a CCD camera (Princeton Instruments, PIX-256E) connected to a monochromator (Princeton Instruments, HRS-300S). The SiO_2/Si substrate was glued to the holder in the vacuum chamber via a cryogenic adhesive and then dried for ≈12 h to ensure that the solvents in the cryogenic adhesive were completely evaporated and the freshly exfoliated samples on adhesive tape were then transferred to the SiO_2/Si substrate on the holder in a glove box. For the measurements of lasing performance, the samples were kept at 80 K inside a vacuum chamber. Before testing, the vacuum level was maintained $<10^{-4}$ Pa. For $(PEA)_2SnI_4$, the excitation light wavelength is 530 nm, and for $(PEA)_2MASn_2I_7$ and $(PEA)_2MA_2Sn_3I_{10}$, the excitation light wavelength is 620 nm.

Characterizations: The PXRD measurements were performed with a Bruker D8 Advance instrument, using a copper target. The PL measurement was conducted in the Witec system using a 532 nm laser for excitation. The lifetime was recorded in the Witec system using a 405 nm laser (PDL 800-D, 50 ps, 20 MHz). The UV–vis absorption spectra were collected with a CRAIC 20/30PV Pro instrument. X-ray photoelectron spectroscopy (XPS) was performed using ESCALAB Xi+, using a 500 µm diameter analysis area with a probing depth of 5–10 nm, and the calibration peak energy with C 1s is 284.8 eV. All NMR experiments (^{13}C) were performed at 25 °C on a Bruker NEO 500 MHz NMR spectrometer equipped with a BBO Cryoprobe. Dried DMSO-d_6 was used as the solvent.

FIB Fabrication: The perovskite arrays were fabricated via a focused ion beam scanning electron microscope (FIB-SEM) with a Ga ion source. It was crucial to transfer and load samples in a glove box filled with inert gas to prevent oxidation. Moreover, the exposure time of the samples was minimized under the electron beam to reduce potential damage and use low-dose etching to decrease the impact depth of Ga ion on the edges. When the array was designed, the etched area by the FIB was minimized. To maintain a high proportion of undamaged perovskite, the side length or diameter should be greater than 3 µm. This ensures that a significant portion of the material remains intact, preserving its structural and functional integrity.

Computational Methods—Bader Analysis: The charge-neutral SnI_4 terminated surface was used to perform the Bader analysis. The charge density (CHGCAR) files were generated from the VASP[41,42] calculations by setting LAECHG = TRUE to incorporate the core charge.[43,44] The cut-off energy for the plane wave basis functions was set to 700 eV. The generalized gradient approximation[45] of the Perdew–Burke–Ernzerhof functional for solids (PBEsol)[46] was used for the description of exchange and correlation. During structural relaxation, the perovskite framework remained unrelaxed, and only all atoms in the surface molecules relaxed with Hellmann–Feynman forces below 0.01 eV $Å^{-1}$. The role of spin–orbit coupling (SOC) was not considered in this work. The van der Waals interactions were described via the DFT-D2 method.[47] The Bader charges were calculated via the method of Kelman et al.[48]

Simulated Electrostatic Potential Mapping: The theoretical calculations were performed via the Gaussian 16 suite of programs. The structure of the biuret was fully optimized at the B3LYP-D3BJ/TZVP level of theory. The vibrational frequencies of the optimized structure were carried out at the same level. The structures were characterized as a local energy minimum on the potential energy surface by verifying that all the vibrational frequencies were real. The Gauss View package was used to plot the color-filled isosurface graphs to visualize the molecular electrostatic potential (MESP).

Simulated Electric Field Distributions: The numerical calculation was performed via commercial COMSOL Multiphysics 6.0 software. The waveguide mode properties including the electric field intensity distribution of the $(PEA)_2SnI_4$ single crystal on top of the substrate were calculated via the finite-difference time-domain (FDTD) method.

Supporting Information

Supporting Information is available from the Wiley Online Library or from the author.

Acknowledgements

E.S. acknowledges the financial support from the Research Center for Industries of the Future at Westlake University, National Natural Science Foundation of China (grant no. 52272164). Y.H. acknowledges the financial support from the National Natural Science Foundation of China (grant no. 10311037A012401). This research was partially supported by both the Instrumentation and Service Center for Molecular Sciences and the Instrumentation and Service Center for Physical Sciences at Westlake University. The authors would like to thank D. Gu, and X. Lu from the Instrumentation and Service Center for Molecular Sciences at Westlake University, and Y. Lin from the Instrumentation and Service Center for Physical Sciences at Westlake University for their assistance and discussion.

Conflict of Interest

The authors declare no conflict of interest.

Author Contributions

Y.L. and E.S. conceived the project. Y.L. synthesized single-crystal samples, conducted PXRD, steady-state PL, TRPL, NMR, and XPS measurements, and collected lasing data. Z.L. and A.W. performed the Bader analysis. Y.H. participated in material characterization and data collection. R.L. optimized the lasing test conditions. J.Y. performed the polarization-resolved lasing test. J.Z. performed the simulation of electrostatic potential mapping of biuret molecules. C.L. performed the simulation of electric field distributions. C.L., M.X., H.Z., X.S., B.L., Y.Z., X.S., X.L., and Y.G. participated in data analysis. Y.L. and E.S. wrote the manuscript. All authors read and revised the manuscript.

Data Availability Statement

The data that support the findings of this study are available in the supplementary material of this article.

Keywords

2D tin halide perovskite, lasing, oxidation suppression

Received: December 4, 2024
Revised: February 23, 2025
Published online: March 17, 2025

[1] C. Qin, A. S. D. Sandanayaka, C. Zhao, T. Matsushima, D. Zhang, T. Fujihara, C. Adachi, *Nature* **2020**, *585*, 53.
[2] W. Shao, J. H. Kim, J. Simon, Z. Nian, S.-D. Baek, Y. Lu, C. B. Fruhling, H. Yang, K. Wang, J. Y. Park, L. Huang, Y. Yu, A. Boltasseva, B. M. Savoie, V. M. Shalaev, L. Dou, *Science* **2024**, *384*, 1000.
[3] H. Zhu, Y. Fu, F. Meng, X. Wu, Z. Gong, Q. Ding, M. V. Gustafsson, M. T. Trinh, S. Jin, X. Y. Zhu, *Nat. Mater.* **2015**, *14*, 636.
[4] J. Tian, Q. Y. Tan, Y. Wang, Y. Yang, G. Yuan, G. Adamo, C. Soci, *Nat. Commun.* **2023**, *14*, 1433.
[5] L. Zhang, Y. Wang, A. Chu, Z. Zhang, M. Liu, X. Shen, B. Li, X. Li, C. Yi, R. Song, Y. Liu, X. Zhuang, X. Duan, *Nat. Commun.* **2024**, *15*, 5484.
[6] H. Gu, J. Xia, C. Liang, Y. Chen, W. Huang, G. Xing, *Nat. Rev. Mater.* **2023**, *8*, 533.
[7] S. W. Eaton, M. Lai, N. A. Gibson, A. B. Wong, L. Dou, J. Ma, L.-W. Wang, S. R. Leone, P. Yang, *Proc. Natl. Acad. Sci. USA* **2016**, *113*, 1993.
[8] Y. Li, H. Zhou, M. Xia, H. Shen, T. Wang, H. Gao, X. Sheng, Y. Han, Z. Chen, L. Dou, H. Zhu, E. Shi, *Sci. Adv.* **2023**, *9*, eadh0517.
[9] X. Wang, L. Jin, A. Sergeev, W. Liu, S. Gu, N. Li, K. Fan, S.-c. Chen, K. S. Wong, X. Sun, N. Zhao, *Sci. Adv.* **2023**, *9*, eadj3476.
[10] Y. Liang, Q. Shang, Q. Wei, L. Zhao, Z. Liu, J. Shi, Y. Zhong, J. Chen, Y. Gao, M. Li, X. Liu, G. Xing, Q. Zhang, *Adv. Mater.* **2019**, *31*, 1903030.
[11] A. L. Alvarado-Leaños, D. Cortecchia, C. N. Saggau, S. Martani, G. Folpini, E. Feltri, M. D. Albaqami, L. Ma, A. Petrozza, *ACS Nano* **2022**, *16*, 20671.
[12] Y. Jia, R. A. Kerner, A. J. Grede, B. P. Rand, N. C. Giebink, *Nat. Photonics* **2017**, *11*, 784.
[13] Q. Zhang, S. T. Ha, X. Liu, T. C. Sum, Q. Xiong, *Nano Lett.* **2014**, *14*, 5995.
[14] C. C. Stoumpos, D. H. Cao, D. J. Clark, J. Young, J. M. Rondinelli, J. I. Jang, J. T. Hupp, M. G. Kanatzidis, *Chem. Mater.* **2016**, *28*, 2852.
[15] B. Saparov, D. B. Mitzi, *Chem. Rev.* **2016**, *116*, 4558.
[16] Y. Gao, E. Shi, S. Deng, S. B. Shiring, J. M. Snaider, C. Liang, B. Yuan, R. Song, S. M. Janke, A. Liebman-Peláez, P. Yoo, M. Zeller, B. W. Boudouris, P. Liao, C. Zhu, V. Blum, Y. Yu, B. M. Savoie, L. Huang, L. Dou, *Nat. Chem.* **2019**, *11*, 1151.
[17] K. Leng, I. Abdelwahab, I. Verzhbitskiy, M. Telychko, L. Chu, W. Fu, X. Chi, N. Guo, Z. Chen, Z. Chen, C. Zhang, Q.-H. Xu, J. Lu, M. Chhowalla, G. Eda, K. P. Loh, *Nat. Mater.* **2018**, *17*, 908.
[18] X. Gong, O. Voznyy, A. Jain, W. Liu, R. Sabatini, Z. Piontkowski, G. Walters, G. Bappi, S. Nokhrin, O. Bushuyev, M. Yuan, R. Comin, D. McCamant, S. O. Kelley, E. H. Sargent, *Nat. Mater.* **2018**, *17*, 550.
[19] M. Yin, H. Yao, H. Qiu, C. Wu, M. Zhang, F. Hao, *Adv. Funct. Mater.* **2024**, *34*, 2404792.
[20] F. Yuan, G. Folpini, T. Liu, U. Singh, A. Treglia, J. W. M. Lim, J. Klarbring, S. I. Simak, I. A. Abrikosov, T. C. Sum, A. Petrozza, F. Gao, *Nat. Photonics* **2024**, *18*, 170.
[21] D. Yu, M. Pan, G. Liu, X. Jiang, X. Wen, W. Li, S. Chen, W. Zhou, H. Wang, Y. Lu, M. Ma, Z. Zang, P. Cheng, Q. Ji, F. Zheng, Z. Ning, *Nat. Energy* **2024**, *9*, 298.
[22] D. Han, J. Wang, L. Agosta, Z. Zang, B. Zhao, L. Kong, H. Lu, I. Mosquera-Lois, V. Carnevali, J. Dong, J. Zhou, H. Ji, L. Pfeifer, S. M. Zakeeruddin, Y. Yang, B. Wu, U. Rothlisberger, X. Yang, M. Grätzel, N. Wang, *Nature* **2023**, *622*, 493.
[23] X. Li, Y. Guan, X. Li, Y. Fu, *J. Am. Chem. Soc.* **2022**, *144*, 18030.
[24] C. M. M. Soe, G. P. Nagabhushana, R. Shivaramaiah, H. Tsai, W. Nie, J.-C. Blancon, F. Melkonyan, D. H. Cao, B. Traoré, L. Pedesseau, M. Kepenekian, C. Katan, J. Even, T. J. Marks, A. Navrotsky, A. D. Mohite, C. C. Stoumpos, M. G. Kanatzidis, *Proc. Natl. Acad. Sci. USA* **2019**, *116*, 58.
[25] L. Mao, R. M. Kennard, B. Traore, W. Ke, C. Katan, J. Even, M. L. Chabinyc, C. C. Stoumpos, M. G. Kanatzidis, *Chem* **2019**, *5*, 2593.
[26] J. Y. Park, R. Song, J. Liang, L. Jin, K. Wang, S. Li, E. Shi, Y. Gao, M. Zeller, S. J. Teat, P. Guo, L. Huang, Y. S. Zhao, V. Blum, L. Dou, *Nat. Chem.* **2023**, *15*, 1745.
[27] Z. Shi, F. Zhang, J. Yan, Y. Zhang, X. Chen, S. Chen, D. Wu, X. Li, Y. Zhang, C. Shan, *Nano Res.* **2022**, *15*, 492.
[28] K.-Y. Cheng, *Compound Semiconductors and Devices*, Springer, Berlin, Germany, **2020**.
[29] Y. Fu, H. Zhu, J. Chen, M. P. Hautzinger, X. Y. Zhu, S. Jin, *Nat. Rev. Mater.* **2019**, *4*, 169.
[30] L. Lanzetta, T. Webb, N. Zibouche, X. Liang, D. Ding, G. Min, R. J. E. Westbrook, B. Gaggio, T. J. Macdonald, M. S. Islam, S. A. Haque, *Nat. Commun.* **2021**, *12*, 2853.

[31] H. Jia, H. Shi, R. Yu, H. Ma, Z. Wang, C. Zou, Z. a. Tan, *Small* **2022**, *18*, 2200036.
[32] X. Luo, R. Hao, H. Wang, W. Zhai, Z. Wang, Z. Ning, Y. Yu, *J. Phys. Chem. C* **2023**, *127*, 11632.
[33] T. Wang, Y. Fu, L. Jin, S. Deng, D. Pan, L. Dong, S. Jin, L. Huang, *J. Am. Chem. Soc.* **2020**, *142*, 16254.
[34] L. Zhao, Z. Shi, Y. Zhou, X. Wang, Y. Xian, Y. Dong, O. Reid, Z. Ni, M. C. Beard, Y. Yan, J. Huang, *Nat. Photonics* **2024**, *18*, 250.
[35] P. You, G. Li, G. Tang, J. Cao, F. Yan, *Energy Environ. Sci.* **2020**, *13*, 1187.
[36] J. S. Manser, P. V. Kamat, *Nat. Photonics* **2014**, *8*, 737.
[37] J. Lim, M. T. Hörantner, N. Sakai, J. M. Ball, S. Mahesh, N. K. Noel, Y.-H. Lin, J. B. Patel, D. P. McMeekin, M. B. Johnston, B. Wenger, H. J. Snaith, *Energy Environ. Sci.* **2019**, *12*, 169.
[38] C. H. Henry, R. A. Logan, K. A. Bertness, *J. Appl. Phys.* **1981**, *52*, 4457.
[39] I. S. Grudinin, A. B. Matsko, A. A. Savchenkov, D. Strekalov, V. S. Ilchenko, L. Maleki, *Opt. Commun.* **2006**, *265*, 33.
[40] M. Li, Y. He, X. Feng, W. Qu, W. Wei, B. Yang, H. Wei, *Adv. Mater.* **2023**, *35*, 2307042.
[41] G. Kresse, J. Hafner, *Phys. Rev. B* **1993**, *47*, 558.
[42] G. Kresse, J. Furthmüller, *Phys. Rev. B* **1996**, *54*, 11169.
[43] P. E. Blöchl, *Phys. Rev. B* **1994**, *50*, 17953.
[44] G. Kresse, D. Joubert, *Phys. Rev. B* **1999**, *59*, 1758.
[45] J. P. Perdew, K. Burke, M. Ernzerhof, *Phys. Rev. Lett.* **1996**, *77*, 3865.
[46] G. I. Csonka, J. P. Perdew, A. Ruzsinszky, P. H. T. Philipsen, S. Lebègue, J. Paier, O. A. Vydrov, J. G. Ángyán, *Phys. Rev. B* **2009**, *79*, 155107.
[47] S. Grimme, *J. Comput. Chem.* **2006**, *27*, 1787.
[48] W. Tang, E. Sanville, G. Henkelman, *J. Phys.:Condens. Matter* **2009**, *21*, 084204.